J. Fluid Mech. (1994), *vol.* 265, *pp.* 97–124

Molecular mixing in Rayleigh–Taylor instability

By P. F. LINDEN[1], J. M. REDONDO[2] AND D. L. YOUNGS[3]

[1] Department of Applied Mathematics and Theoretical Physics, University of Cambridge, Silver Street, Cambridge CB3 9EW, UK

[2] Departamento Fisica Aplicada, Universitat Politecnica de Catalunya, c/Jordi Girona 31, Barcelona 08034, Spain

[3] Atomic Weapons Establishment, Aldermaston, Reading RG7 4PR, UK

(Received 13 July 1992 and in revised form 7 October 1993)

Mixing produced by Rayleigh–Taylor instability at the interface between two layers is the subject of a comparative study between laboratory and numerical experiments. The laboratory experiments consist of a layer of brine initially at rest on top of a layer of fresh water. When a horizontal barrier separating the two layers is removed, the ensuing motion and the mixing that is produced is studied by a number of diagnostic techniques. This configuration is modelled numerically using a three-dimensional code, which solves the Euler equations on a 180^3 grid. A comparison of the numerical results and the experimental results is carried out with the aim of making a careful assessment of the ability of the code to reproduce the experiments. In particular, it is found that the motions are quite sensitive to the presence of large scales produced when the barrier is removed, but the amount and form of the mixing is not very sensitive to the initial conditions. The implications of this comparison for improvements in the experimental and numerical techniques are discussed.

1. Introduction

Rayleigh–Taylor instability is one of the prime candidates for mixing between fluids of different densities. It occurs when the fluids are arranged so that higher pressure occurs in the less dense fluid. The simplest case to consider is that of a fluid in a gravitational field in which the density decreases in the direction of gravity. Then with the dense fluid above the less dense fluid, gravitational instability ensues in the form of Rayleigh–Taylor instability. This mechanism occurs in stably stratified fluids when density surfaces are overturned such as in a large-amplitude internal wave. Many other examples exist both in geophysical and in industrial applications when other forms of acceleration may produce the required pressure gradients. In most of these practical circumstances the instability that is produced occurs at sufficiently fast speeds that the flow develops on a range of lengthscales and rapidly becomes turbulent. If the fluids are miscible, the generation of turbulence will promote mixing at a molecular level. This paper is part of a sequence of papers which have been written to investigate these effects. The overall aim of this study has been to investigate the mixing process produced by Rayleigh–Taylor instabilities, with a view to providing an explanation for the observed mixing rates in these flows.

The configuration chosen for the experimental study is the instability produced between two layers of fluid with the dense fluid above, separated by a horizontal plane boundary. The instability is initiated by removing a barrier between the two fluids and allowing the gravitationally driven instabilities to occur. The fluids chosen were salt

solutions in water, and are therefore completely miscible, and the density ratios between the two fluids are close to unity. The global structure of the mixing zone was described in Linden & Redondo (1991, referred to hereafter as LR). These studies showed that the mixing region grew with a width which was proportional to gt^2, where g is the acceleration due to gravity and t is the elapsed time, and the growth rate was determined for a range of density ratios. The development of small scales, which contribute to the mixing, was determined by measuring the fractal dimension of the interface along an iso-concentration line. It was observed that the fractal dimension increased as small scales developed, reaching a maximum value of 2.35, and then decreased again as the fluids overturned and the stratification became stable. The efficiency of the mixing process was also measured by evaluating the change in potential energy between the initial and final states. High values of the mixing efficiency were measured, and this was attributed to the fact that much of the mixing took place while the flow was unstably stratified.

There have been many two-dimensional calculations of Rayleigh–Taylor instability. Early results were published by Harlow & Welch (1966) and Daly (1967). More recent calculations are described by Youngs (1984), Tryggvason (1988) and Kerr (1988). A number of articles have been published by Glimm and his co-workers (Chern *et al.* 1986; Glimm *et al.* 1990); these papers used an interface tracking method and focused on the increase in the lengthscale associated with the mixing zone, due to interactions between bubbles of light fluid.

Few simulations of Rayleigh–Taylor instability in three dimensions have been published. The growth of the instability from a single-wavelength initial perturbation has been considered by Dahlburg & Gardner (1990), Tryggvason & Unverdi (1990) and Town & Bell (1991). Three-dimensional calculations of turbulent mixing by Rayleigh–Taylor instability have been performed by Youngs (1991). These calculations were for a range of density ratios and used mesh sizes up to $240 \times 160 \times 160$. The results showed that the growth rate of the mixing zone was smaller than observed in the experiments reported in LR or in earlier experiments by Read (1984). Other aspects of the flow, such as the magnitude of the concentration fluctuations, were found to be in good agreement with the experimental observations of LR.

There have been a number of previous experimental studies of Rayleigh–Taylor instability, which have concentrated primarily on the scale and growth of disturbances at the interface. These include Lewis (1950) and Allred & Blount (1953) using an air–water interface, while other experiments (e.g. Duff, Harlow & Hirt 1962 and Emmons, Chang & Watson 1960) have investigated some other aspects of Rayleigh–Taylor instability. The turbulent mixing regime, in which the width of the mixing zone is proportional to gt^2, has been studied by Anuchina *et al.* (1978), Read (1984), Youngs (1989) and Rozanov *et al.* (1990). In LR we reported on experiments which concentrated on the mixing process, and this present paper is an extension of that work. As was mentioned above, the two fluids are miscible and separated by a horizontal barrier, and the removal of this barrier, which takes place through the sidewalls of the tank, causes a perturbation to the interface. A purpose of this present paper is to make detailed comparisons between the experimental results and calculations which include the effects of this initial perturbation. We shall show that the growth rate of the mixing zone is affected by the presence of the initial perturbation produced by the removal of the barrier for large times when it would have been desirable that the initial memory should have been forgotten. We also make detailed comparisons of the concentration fluctuations and amount of molecular mixing in the

presence and absence of the perturbation, and show how these results are not particularly sensitive to this perturbation.

The layout of this paper is as follows. In §2 the experimental procedure and the numerical calculations are outlined. As these have been reported in considerable detail elsewhere (LR; Youngs 1991) only a brief description will be given here. In §3, the theory of single-wavelength Rayleigh–Taylor instability is reviewed, and used to assess the effect of the additional perturbation induced by barrier removal. Section 4 then gives a comparison of the qualitative structures of the flows that have been observed both in the experiments and in the numerical calculations. Quantitative comparisons of the results are given in §§5 and 6. The global effects such as the mixing-zone growth rate, the volume fractions of the two fluids averaged across horizontal planes and the global mixing efficiencies of the process are compared in §5, while local effects such as the concentration fluctuations, the mixing on small scales, and fractal analysis are described in §6. Some more detailed numerical results corresponding to the ideal experiment in which the perturbation caused by the barrier is absent are given in §7. The summary and conclusions are given in §8.

2. Experiments and the numerical code

The experiments were carried out in a Perspex tank 500 mm deep, 400 mm long and 200 mm wide. The tank had a removable, horizontal aluminium barrier 1.5 mm in thickness, which separated a layer of brine, density ρ_1, from a layer of fresh water, density ρ_2, below. The two layers of fluid were initially at rest, and the experiment was initiated by sliding the aluminium barrier horizontally through a slit in one endwall of the tank. The details of the experimental set-up and, in particular, the measurement techniques are described in detail in LR, and the interested reader is referred to that paper for further information. Figure 1 shows a schematic diagram of the tank used in the experiments and the notation used to describe the advance of the Rayleigh–Taylor front.

The experiments were conducted with a range of Atwood numbers $A = (\rho_1-\rho_2)/(\rho_1+\rho_2)$ from 1×10^{-4} to 5×10^{-2}. If the mixing zone width is proportional to gt^2, then velocities are proportional to gt and the Reynolds number Re increases with time t like t^3. For the range of Atwood numbers used here Re reaches a value $O(10^8)$ by the time the first upper-layer fluid reaches the bottom of the tank. The use of salt in water implies that the Schmidt number Sc is high, of $O(10^3)$.

Measurements of the amount of mixed product were obtained using the colour change of a pH indicator to determine the extent of a chemical reaction. The lower layer contained an acid (HCl) and the pH indicator phenolphthalein which was initially colourless. The upper (also colourless) layer was set at a required high pH by the addition of an alkali (NaOH). When mixing between the upper and lower layer fluids occurs and the pH of the mixture exceeds the threshold for phenolphthalein (pH $\approx$ 9.5), the indicator turns pink. The intensity of the pink colour is a function of the concentration of phenolphthalein in the mixture. By suitable choices of the pH in the lower layer it is possible to adjust the fraction of upper-layer fluid that mixes with the lower layer in order to exceed the threshold pH. In order to ensure a rapid colour change, the pH of the upper layer was set to a high value (pH = 12). The concentration of phenolphthalein was then determined by measuring the reduction in intensity of light passing through the tank. Light intensity measurements are made using the automated image processing system DigImage. The reaction between the indicator and

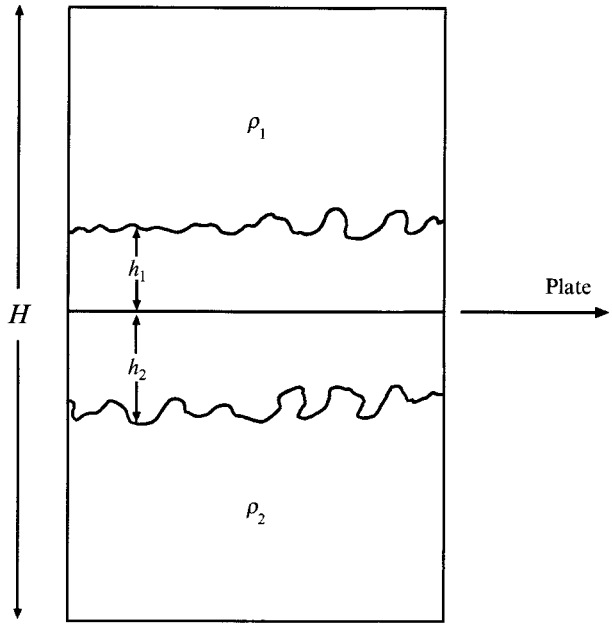

FIGURE 1. A sketch of the experimental configuration. The symbols are defined in the text.

NaOH is extremely fast (the Damköhler number, which is the ratio of the advective timescale of the flow to the reaction time, is very large) and so is limited only by the rate of mixing of the two constituent parts (see Caldin 1964; and RL).

The numerical technique used here is the same as that described by Youngs (1991). An explicit compressible method is used to solve the Euler equations plus an advection equation for the mass fraction of fluid 1. The experiments, in which the flow is incompressible, are simulated by choosing the initial sound speed high enough to eliminate any dependence on Mach number. In the problem considered here there is an initial discontinuity in the density distribution. It is therefore important to choose a numerical method which can cope with discontinuities. Hence advection of all fluid variables is calculated by using the monotonic method of van Leer (1977). This gives a robust numerical method with many essential properties, for example mass fractions remain in the interval (0, 1) and the fluid density stays in the interval (ρ_2, ρ_1). Spurious buoyancy-generated turbulence is thereby eliminated. The need to use a monotone advection scheme for this reason has also been recognized by Grabowski & Clark (1991) in simulations of convective clouds.

The laboratory experiments described here used miscible fluids and a high degree of molecular mixing was observed. Consequently, the numerical method needs to include a mechanism for the dissipation of both density and velocity fluctuations due to small-scale eddies. In large-eddy simulations, such as those of Moin & Kim (1982), a non-dissipative numerical technique is used in conjunction with a sub-grid eddy viscosity to represent the effect of the unresolved scales. In the present calculations, the monotonicity constraints in the advection method provide the required dissipation for both density and velocity fluctuations. No additional dissipation is needed. The nonlinear dissipation inherent in the numerical scheme acts at a lengthscale of order of the mesh size; the effect on the resolved scales is negligible. Hence there is a similarity with the use of hyperviscosity in spectral methods for direct numerical simulation of turbulent flow (see, for example, Passot & Pouquet 1988). Results for homogeneous turbulence show that a $k^{-\frac{5}{3}}$ Kolmogorov spectrum is obtained up to a wavenumber

$k = 2\pi/\lambda_c$, where λ_c is about six mesh widths. The spectrum decays more rapidly than $k^{-\frac{5}{3}}$ above this point. For the present application an example of the power spectrum for concentration fluctuations is shown in figure 14. The dissipation inherent in the numerical scheme is clearly sufficient to prevent any piling-up of power levels at high wavenumbers. As for homogeneous turbulence, the spectrum is consistent with a $k^{-\frac{5}{3}}$ flow up to the point where the wavelength is about 6 mesh widths. Large-eddy simulation with the use of a sub-grid model may give a better representation of a $k^{-\frac{5}{3}}$ spectrum than this. However, the monotone advection scheme has a number of other advantages, as already noted.

The numerical Schmidt number, Sc, is of order unity whereas in the experiments $Sc \sim 10^3$. If there is dependence of the results on the Schmidt number, it cannot be resolved in the numerical calculations. At low Reynolds number, a high Schmidt number will inhibit molecular mixing. However, at high Reynolds number the generation of fine scales in the turbulence suggests that molecular mixing may be less sensitive to the Schmidt number. The experimental results obtained with the chemical indicator (see §6.2) show that a high degree of molecular mixing has occurred by the time the mixing zone has reached the top of the tank. Consequently, we infer that comparison of the molecular mixing in the numerical calculations and the experiments is reasonable, although further investigation of this point is desirable.

The initial set-up for the numerical calculations is the same as that used by Youngs (1991). The computational domain is $0 < x, y < H$, $-\frac{1}{2}H < z < \frac{1}{2}H$ where H is the height of the tank. Fluid of density ρ_1 fills the upper half of the box, $z > 0$, and fluid of density $\rho_2 < \rho_1$ fills the lower half. The boundary conditions are zero normal velocity at the top and bottom of the tank, and periodic behaviour in the x- and y-directions. The density ratio used is $\rho_1/\rho_2 = 1.5$. This value, which is higher than in the experiments, is chosen to ensure that the initial density difference is large compared to any small density variations within each fluid arising from the use of finite Mach number. Within the limitations of the Boussinesq approximation, comparison can be made with experiment by choice of an appropriate timescale.

A random initial interface perturbation is included in all the calculations. This consists of a sum of Fourier modes with minimum wavelength, λ_{min}, four times the mesh width, Δx. In the first calculations performed, the standard deviation of the random perturbation was $\sigma = 0.08\Delta x = 4 \times 10^{-4} H$, which is just sufficient to trigger the gt^2 growth of the mixing zone (see §3). Two different mesh sizes, 90^3 and 180^3, have been used and the effects of reducing the mesh are examined.

Removal of the barrier induces a long-wave two-dimensional perturbation, as is evident from the flow visualization, figure 2(*c*). It is shown in the next section that this perturbation should significantly enhance the mixing rate, and it therefore needs to be included in the simulation. The approximate effect of barrier removal is represented by an extra perturbation $z = \zeta(x)$ given by

$$\zeta(x) = a_0 \cos(2\pi x/\lambda),$$

with values for the wavelength $\lambda = H/6 = 83$ mm and the amplitude $a_0 = 0.01H$ or $0.02H$ chosen by visual comparison with the experiments. For these initial amplitudes the long-wave perturbation grows quickly and the results are not very sensitive to the change in a_0. Barrier removal also creates small-scale turbulence which has been modelled in some of the calculations by increasing the standard deviation of the random perturbation to $\sigma = 0.002H$.

Inclusion of the long-wave perturbation represents the main effects of barrier removal, which are the early appearance of large-scale structures and an enhanced

mixing rate. However, the experimental situation is complex and difficult to model exactly. In the experiments the long-wave perturbation varies in amplitude in the direction of barrier removal. The finite time taken to remove the barrier has some effect on the results, and circulation is induced in the two halves of the tank which influences the late-time overturning motion of the two fluids. The long-wave perturbation included in the calculations gives rise to large-scale features that are more coherent than in the experiment. As the observed structures are more irregular, some aspects of the experiment resemble more closely the calculations using only the random perturbation. The experimental data are compared to both types of calculation, i.e. with and without the long-wave perturbation. The aim of this paper is to show that a combination of laboratory and numerical results may be used to investigate the mixing process rather than to seek exact agreement between simulation and experiment.

3. Theoretical picture

The dominant lengthscale should increase as the mixing zone grows, as described for example by Youngs (1984). For the present purposes the mixing zone may be thought of as the region containing fluid originally from both layers, and the width is its vertical extent. A more precise definition is given in §4. The structures corresponding to the dominant wavelength at a given time may have evolved either (*a*) from the nonlinear interaction between smaller structures, or (*b*) directly from an initial perturbation at the corresponding wavelength. If (*a*) applies then it is likely that loss of memory of the initial conditions will eventually occur. Dimensional reasoning then suggests that, for the high-Reynolds-number case, the mixing zone should be described by a similarity solution with lengthscale proportional to gt^2 (see Belen'kii & Fradkin 1965; Anuchina *et al.* 1978; Youngs 1984). The width δ of the mixing zone should then be given by

$$\delta = f(\rho_1/\rho_2)\, gt^2. \tag{3.1}$$

The experiments of Read (1984) and Youngs (1989), in which no deliberately imposed initial perturbations were present, confirmed equation (3.1). The depth to which the mixing zone penetrated the denser fluid 1 was found to be given by

$$h_1 = \alpha \frac{\rho_1 - \rho_2}{\rho_1 + \rho_2} gt^2, \tag{3.2}$$

where α was approximately 0.06 at all density ratios. If h_2 denotes the depth to which the mixing zone penetrates fluid 2, then h_2/h_1 was shown to be a slowly increasing function of the density ratio ρ_1/ρ_2. In the Boussinesq limit considered in the present experiments, i.e. ρ_1/ρ_2 close to unity, $h_2/h_1 = 1$. The numerical calculations which use $\rho_1/\rho_2 = 1.5$ give $h_2/h_1 \approx 1.1$, a slight deviation from this Boussinesq limit.

In the Boussinesq approximation, the equation for fluid velocity includes a buoyancy source $S = (\rho - \rho_0) g/\rho_0$ where ρ_0 is a reference density. If ρ_0 is set equal to $\frac{1}{2}(\rho_1 + \rho_2)$, then at the start of the experiment $S = Ag$ in the upper layer and $S = -Ag$ in the lower layer, where $A = (\rho_1 - \rho_2)/(\rho_1 + \rho_2)$ is the Atwood number. The experimental behaviour is determined by the product Ag and results presented below are given in the terms of non-dimensional time units τ defined by

$$\tau = (Ag/H)^{\frac{1}{2}} t. \tag{3.3}$$

If (3.2) applies, then the mixing zone just fills the tank when $h_1 = \frac{1}{2}H$, i.e. when $\tau = 1/(2\alpha)^{\frac{1}{2}} \approx 2.9$. After this time, overturning of the two fluids occurs, a stable stratification is set up and eventually density and velocity fluctuations decay to zero. Experimental

and numerical results are presented up to $\tau = 10$, in order to investigate the late-stage behaviour during both the unstably and stably stratified regimes.

As noted in the previous section, removal of the barrier in the experiments induces a large perturbation with wavelength $\lambda \sim 80$ mm and initial amplitude a_0 about 10 mm. In this case the dominant structures evolve directly from the initial perturbation rather than from the interaction between shorter-wavelength modes, at least in the initial stages.

We first consider the growth of a two-dimensional perturbation. Layzer (1955) showed that for an initial perturbation

$$\zeta(x) = a_0 \cos(2\pi x/\lambda),$$

at density ratio $\rho_1/\rho_2 = \infty$, i.e. $A = 1$, the bubble penetration, h_1, both in the linear and nonlinear regimes, could be represented by the model equations

$$\left.\begin{aligned} \mathrm{d}h_1/\mathrm{d}t &= V, \\ (2+E)\,\mathrm{d}V/\mathrm{d}t &= g(1-E) - C_D V^2/\lambda, \\ E &= \exp[-6\pi h_1/\lambda]. \end{aligned}\right\} \tag{3.4}$$

where

The constant C_D, which may be thought of as a drag coefficient, was equal to 6π. At late times, bubbles rise with constant velocity

$$V_\infty = (g\lambda/C_D)^{\frac{1}{2}} = 0.23(g\lambda)^{\frac{1}{2}}, \tag{3.5}$$

in agreement with the experimental results of Lewis (1950). Two-dimensional calculations of the growth of a single-wavelength perturbation show that at the end of the linear phase for $\rho_1/\rho_2 \leqslant 1.5$, bubbles rise with velocity

$$V_\infty \sim 0.29(g\lambda A)^{\frac{1}{2}}.$$

Although, strictly speaking, Layzer's theoretical model is only applicable to the case $A = 1$, equation (3.4) may be modified empirically for low Atwood numbers (i.e. in the Boussinesq limit) by replacing g with Ag in (3.4) to give

$$(2+E)\,\mathrm{d}V/\mathrm{d}t = Ag(1-E) - C_D V^2/\lambda,$$

and taking the value of the drag coefficient to be

$$C_D = Ag\lambda/V_\infty^2 = 1/0.29^2 \sim 11.9.$$

The model then gives the appropriate late-time bubble velocity, V_∞, and also the correct small-amplitude behaviour:

$$\mathrm{d}^2h_1/\mathrm{d}t^2 = (2\pi Ag/\lambda)\,h_1.$$

An alternative model for the growth of a single-wavelength perturbation was given by Glimm *et al.* (1990). The model used here is somewhat simpler and is considered to be sufficiently accurate for the present purpose.

Now, suppose that the initial perturbation consists of small random perturbations, which on their own would lead to a growth of the mixed layer given by (3.2), plus a long-wave perturbation of wavelength λ and amplitude a_0. The additional perturbation should enhance mixing if the values of h_1 calculated from (3.4) exceed those given by (3.2). In order to estimate the effect of the additional perturbation, (3.4) have been integrated up to the time when $h_1 = \frac{1}{2}\lambda$ and the quantity

$$\alpha^* = (h_1 - a_0)/Agt^2,$$

is found. For a given density ratio, α^* depends only on a_0/λ. For low Atwood number the values calculated are shown in table 1.

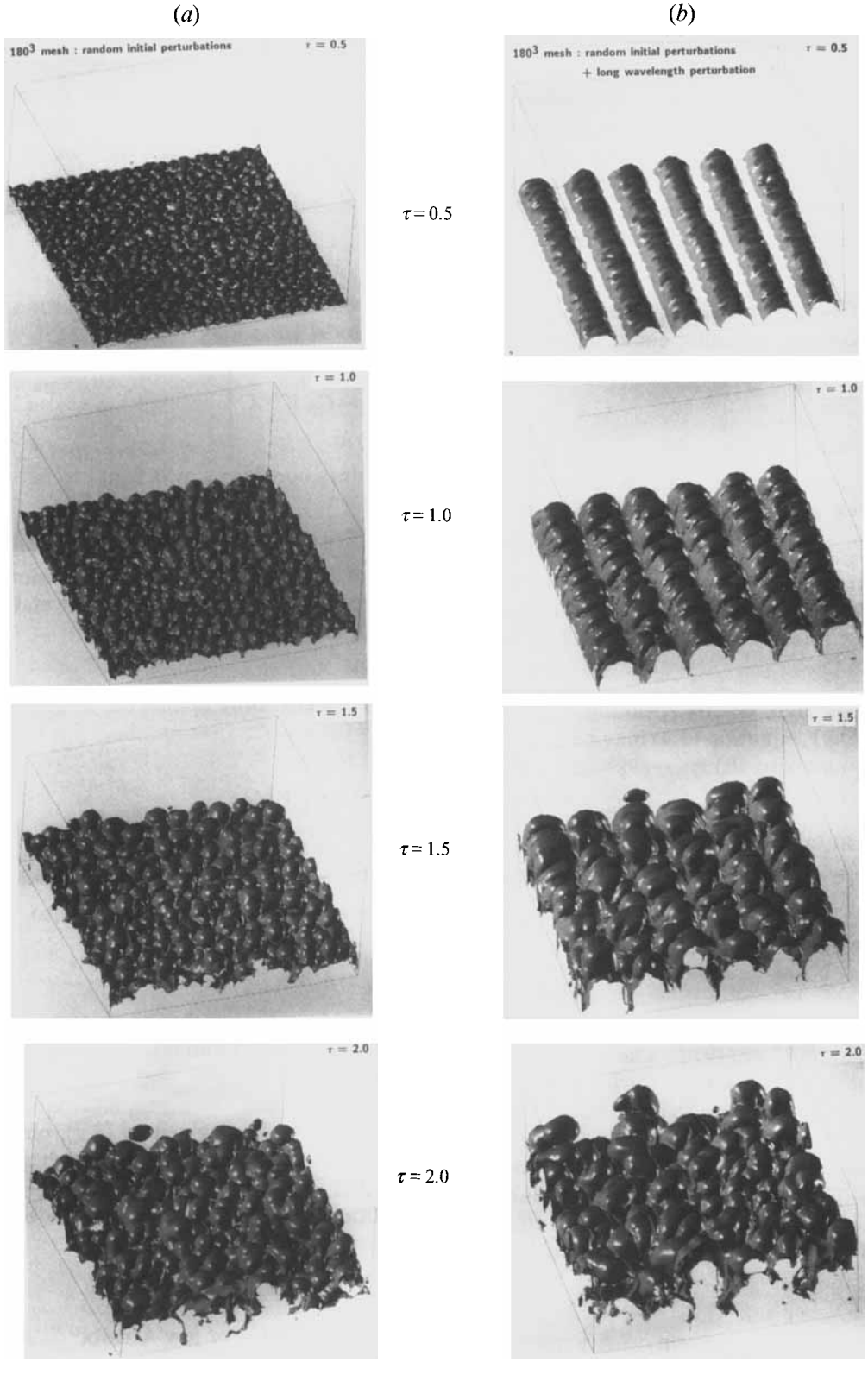

FIGURE 2(*a*, *b*). For caption see facing page.

(*c*)

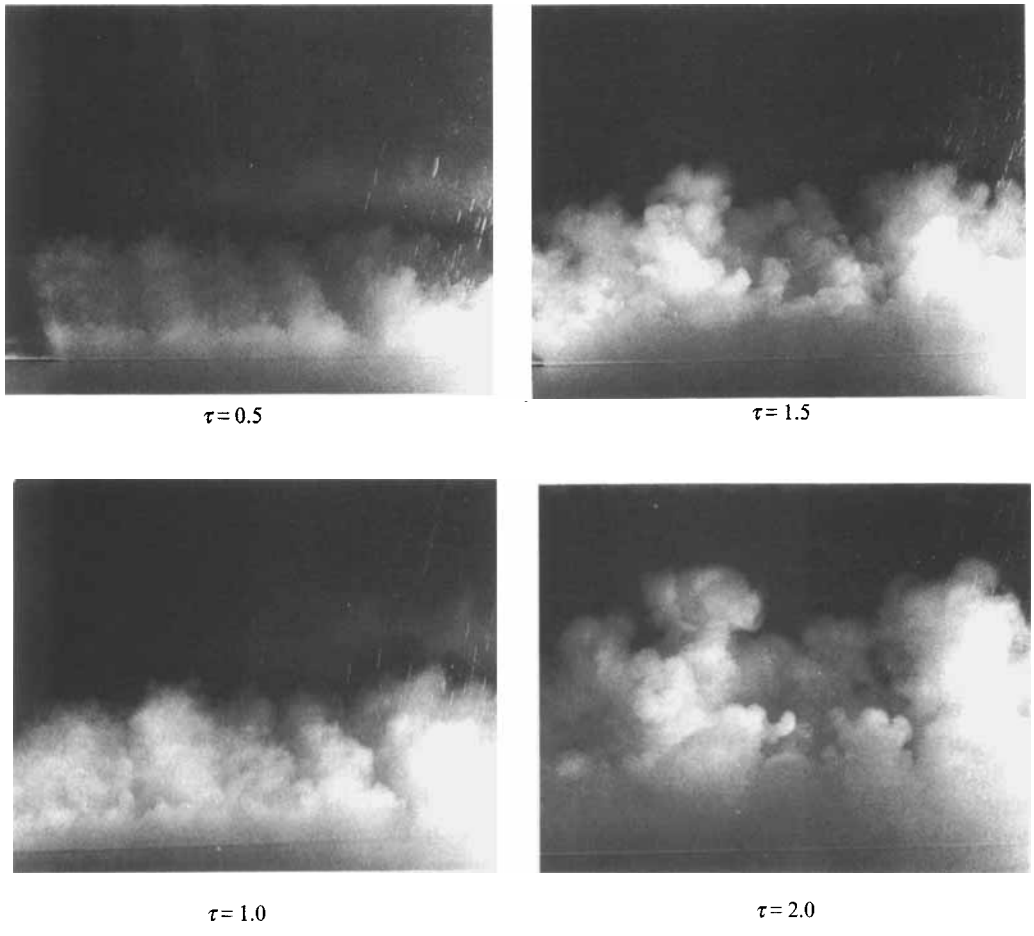

FIGURE 2. Perspective views of the interface in the upper half of the tank at dimensionless times $\tau =$ 0.5, 1.0, 1.5 and 2.0. For the numerical calculations without (*a*) and with (*b*) the long-wave perturbations, surfaces corresponding to $f_1 = 0.99$ are shown. For the experiments (*c*) the lower layer is made visible by the addition of a small amount of milk.

a_0/λ	α^*
0.001	0.035
0.002	0.041
0.005	0.051
0.01	0.061
0.02	0.074
0.05	0.093
0.10	0.11

TABLE 1. The growth rate α^* as a function of the steepness a_0/λ of the initial long-wave perturbation

The estimate of α, obtained from the experiments of Read (1984) and Youngs (1989), is $\alpha = 0.06$. In this case table 1 shows that the additional perturbation should significantly enhance the mixing rate if $a_0/\lambda > 0.01$. It is likely that the additional

perturbation would then influence results until the width of the mixing zone is a few times λ.

For the present experiment, the perturbation introduced by removal of the barrier has $a_0/\lambda \sim 0.06$. Such a perturbation should clearly have a significant effect on the results, leading to an expected increase in the growth of the mixing zone compared with the case when the long-wave disturbance is absent.

4. Qualitative observations

Figures 2(*a*) and 2(*b*) show two sequences of perspective views of the interface obtained from the 180^3 numerical calculations. The surfaces shown correspond to contours of $f_1 = 0.99$, where

$$f_1 = (\rho - \rho_2)/(\rho_1 - \rho_2),$$

denotes the fraction by volume of the denser fluid 1. Only the upper half of the tank $z > 0$ is shown. For the calculation without the long-wave perturbation, small bubbles form at early times. The diameter of these bubbles is between λ_{min} and $2\lambda_{min}$, i.e. their size is set by the mesh resolution. As time proceeds, the characteristic size of the bubbles increases. Figure 2(*b*) shows the effect of including a long-wave perturbation ($a_0 = 0.01H, \lambda = H/6$). At early times the two-dimensional structure arising from the long-wave disturbance clearly dominates the flow. Perturbations grow on the six ridges and by $\tau = 1.5$ each ridge has developed into three-dimensional disturbances, although remnants of the initial two-dimensional structure can be seen. However, the mixing zone at this time is significantly greater than in the calculation without the long-wave perturbation.

A corresponding set of photographs taken from the laboratory experiments is shown in figure 2(*c*). These show a set of perspective views of the top of the lower layer as it penetrates into the upper layer. A small amount of milk has been added to the lower layer which shows up white against the dark background. The views, therefore, correspond to the extreme edge of the advancing lower layer and are equivalent to those shown in figure 2(*b*) from the numerical calculations. (The small, almost vertical, streaks are rising bubbles released from underneath the plate as it is removed.)

The production of a two-dimensional disturbance by the removal of the plate is clearly seen at early times ($\tau = 0.5$) in figure 2(*c*). As the lower layer penetrates further this structure persists, although it begins to be disrupted by smaller-scale three-dimensional motions (see figure 2*c* at $\tau = 1.0$, 1.5, respectively). At later times ($\tau = 2.0$) the motion appears to be quite three-dimensional with thermal-like structures rising from the lower layer. At this stage there still appears to be some residual evidence of the initial two-dimensional perturbation, but the three-dimensional structures have begun to dominate the appearance of the advancing front.

Transition to three-dimensional flow occurs around $\tau = 1.5$ both in the numerical calculations and in the experiments. It is also clear from figure 2(*c*) that further small-scale structures grow on the three-dimensional disturbances. Fractal analysis of these structures has been carried out and are compared to the numerical calculations in §6.

5. Quantitative comparison: global properties

Figure 3 shows the penetration of the lower layer into the upper layer as a function of time. The penetration depth h_1 is non-dimensionalized by the depth of the tank H and $(h_1/H)^{\frac{1}{2}}$ is plotted against the scaled time τ. The value of h_1 is determined by taking the mean value of the 95% concentration level of profiles such as those shown in figure 5. The results in figure 3(*a*) show the numerical calculations both with and without the

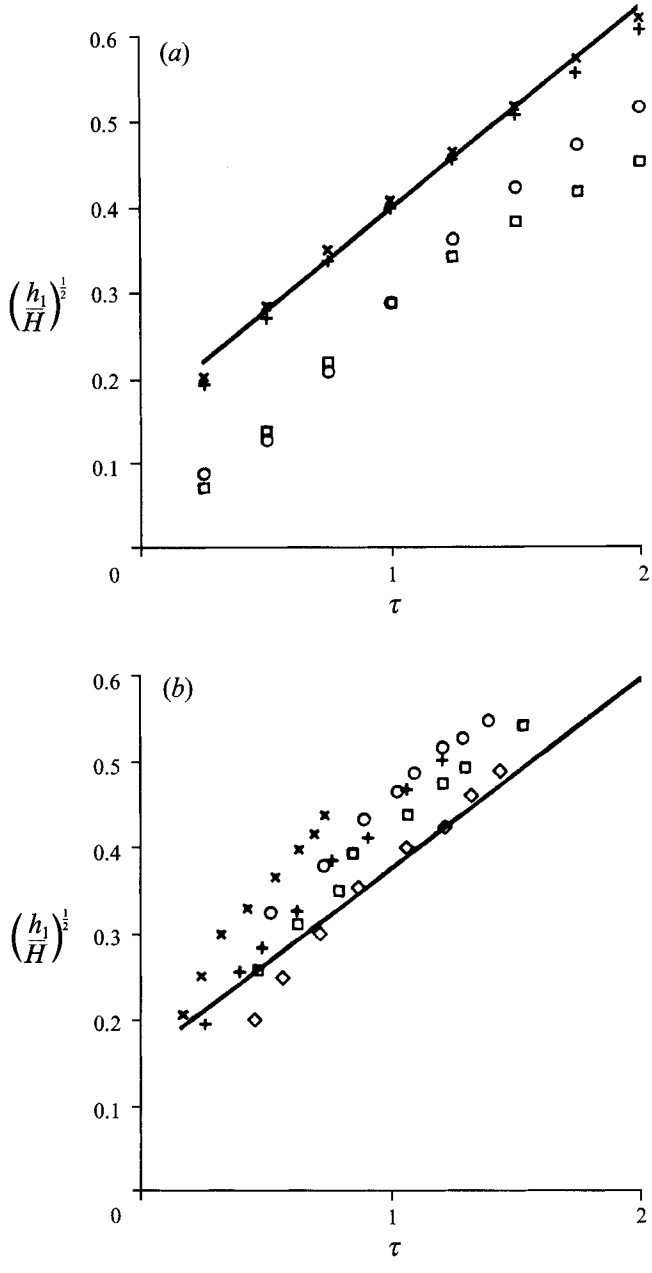

FIGURE 3. A plot of $(h_1/H)^{\frac{1}{2}}$, where h_1 is the distance of penetration of lower-layer fluid into the upper layer, non-dimensionalized by the depth H of the tank, against the dimensionless time τ. (*a*) The numerical calculations for 90^3 mesh and 180^3 mesh, respectively, with (+, ×) and without (○, □) the long-wave perturbation. The solid line is the best fit straight line to the 180^3 mesh data with the long-wave perturbation. (*b*) The experimental results for a range of Atwood numbers: ×, $A = 3.3 \times 10^{-3}$; +, $A = 9.5 \times 10^{-3}$; ○, $A = 2.2 \times 10^{-2}$; □, $A = 3.2 \times 10^{-2}$; ◇, $A = 4.3 \times 10^{-2}$. The solid line is the same line as plotted in (*a*).

long-wave perturbation, as described in §2. We see from this figure that the presence of the long-wave perturbation significantly enhances the growth of the mixed region over the full depth of the tank. The results involving the long-wave perturbation are insensitive to the mesh size. This is because the long-wave perturbation, which has a

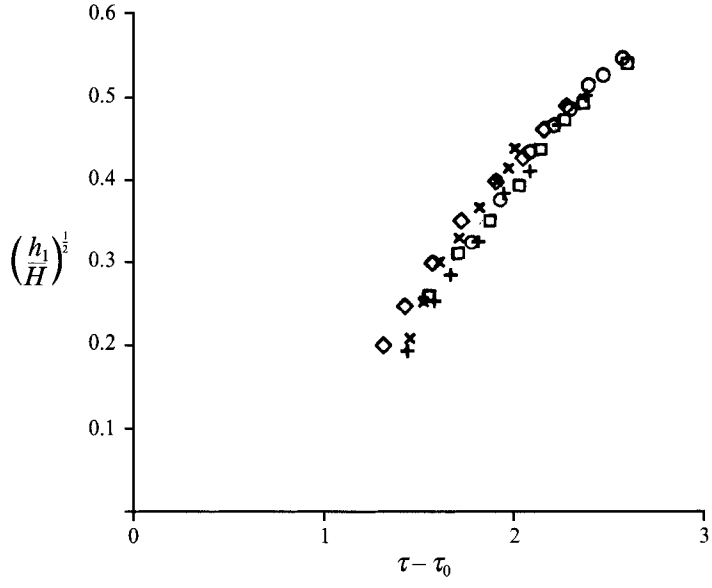

FIGURE 4. The data shown in figure 3(*b*) plotted against $\tau - \tau_0$, where the virtual time origin τ_0 is defined in the text.

dominant effect on the mixing rate, is well resolved by the numerical mesh. It is seen that a straight line fits the data well, with the possible exception of very early times.

On the other hand, the growth without the long-wave perturbation shows dependence on the mesh size. In this case the lengthscale associated with the turbulent mixing zone increases in proportion to t^2. It is inevitable that the early-time behaviour is poorly resolved by the numerical mesh. The effect of mesh size will be discussed in detail in §7. It is found that, at the start of the calculation, when the inertial range cannot be resolved, dissipation is underestimated and the growth rate is too high. The high initial growth rate persists for a longer time in the calculation with the coarser mesh. Hence mixing is more rapid with a coarser mesh. The results of §7 show that the turbulent mixing zone is well resolved when h_1 is 50 meshes. In the fine-mesh calculation, h_1 reaches 90 mesh widths. The mixing process should then be well resolved except at early times.

Figure 3(*b*) is a selection of the experimental points for a decade variation of the Atwood number from 3.3×10^{-3} to 4.3×10^{-2}. Also shown in this figure is the growth from the numerical model with the long-wave perturbation. At later times the experimental results also fall on straight lines when plotted against τ, indicating that the growth of the region of interpenetration of the two layers is in an approximate similarity phase (see LR). The slopes, and hence the growth rates, are in agreement with the numerical calculation when the long-wave perturbation is included. Comparison with figure 3(*a*) shows that the calculations in the absence of the long-wave perturbation significantly under predict the observed growth rate throughout the growth of the mixing region. A time origin τ_0 may be obtained by fitting (using a least-squares fit) a straight line to the data of $(h_1/H)^{\frac{1}{2}}$ against τ, and determining the value τ_0 at which the line intersects the τ-axis. In figure 4 (and all subsequent figures), the data are plotted against $\tau - \tau_0$. This procedure collapses the data and hence is an effective way of parameterizing the initial effects of the plate removal. The value of τ_0 can be thought of as representing the effect of the finite time taken to remove the plate and for the time taken to reach the similarity growth given by (3.2). From these data we estimate $\alpha = 0.044 \pm 0.005$. This value is smaller than we had determined from our

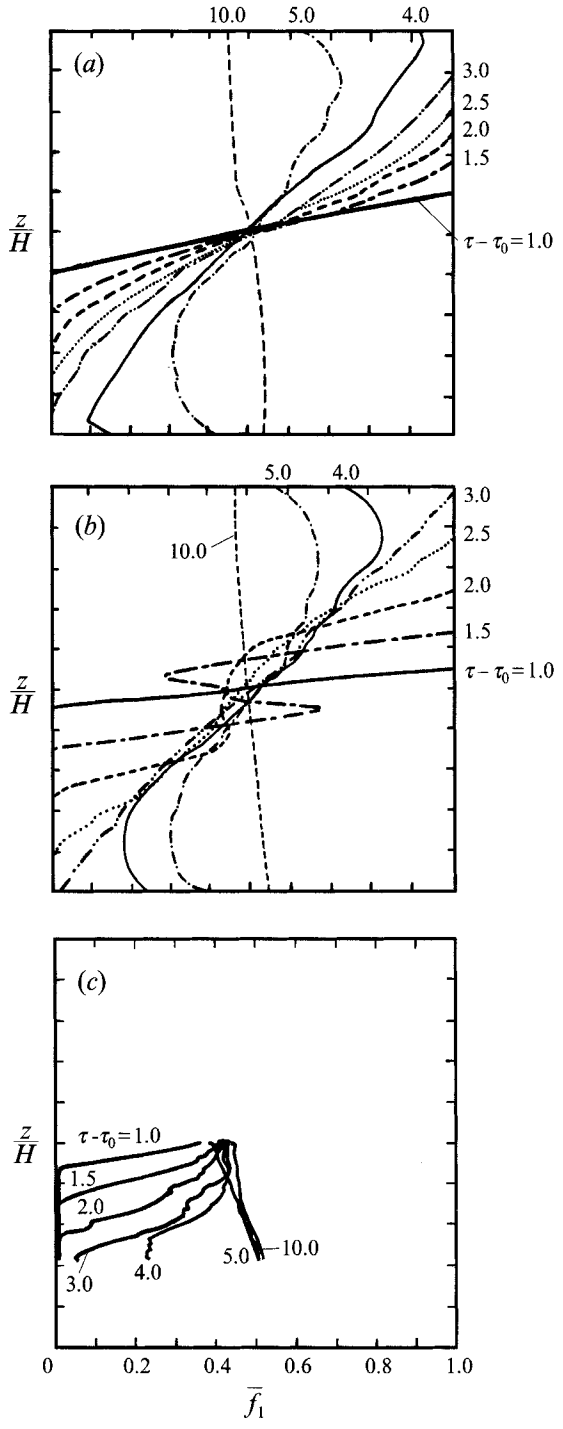

FIGURE 5. Concentration $\overline{f}_1$ of upper-layer fluid averaged over horizontal planes as a function of depth, at selected times $\tau - \tau_0 = 1.0$, 1.5, 2.0, 2.5, 3.0, 4.0, 5.0 and 10.0 during the evolution of the flow. The concentration has been normalized so that the initial concentration of the upper layer is $\overline{f}_1 = 1$. The numerical results are shown in (*a*) without (*b*) with the long-wave perturbation. The experimental results are shown in (*c*).

earlier experiments (LR) and we attribute this difference to the use of the virtual time origin in the present case. It is very difficult to obtain unequivocal fits to data of the type presented in figure 4, particularly when a virtual origin is needed to collapse the data. Hence, this value of α should be treated with caution, but it is we believe the estimate that is most useful to compare with the numerical results as these have been analysed in the same way.

Figure 5 shows the concentration $\overline{f_1}$ of upper-layer fluid averaged over horizontal planes as a function of the depth at selected times during the evolution of the flow. The numerical results are shown in figures 5(*a*) and 5(*b*), and the experimental results are shown in figure 5(*c*). The experimental values are obtained by measuring the absorption of light through a passive dye initially in the upper layer only (see §2). The concentration has been normalized so that the initial concentration of the upper layer is $\overline{f_1} = 1$. In order to obtain sufficient vertical resolution, the experimental measurements were restricted to part of the lower layer, $-0.3 < z/H < 0$. The growth of the penetration region of upper-layer fluid shown in figure 4 is clearly seen from these measurements. At $\tau - \tau_0 = 1.5$ the numerical results including the long-wave perturbation (figure 5*b*) yield a profile that is not monotonic. This feature is a result of large blobs of upper-layer fluid penetrating into the lower layer (and vice versa). As mixing occurs these features decrease and the horizontally averaged concentrations become monotonic with depth. This result is in contrast to the experimental measurements, which show that the profiles remain monotonic at all times. The reason for this discrepancy seems to be that the simple form used to represent the long-wave perturbation in this simulation is more coherent than in the experiment. At $\tau - \tau_0 \approx 3$ the upper layer has penetrated to the bottom of the tank (see also figure 4). It is important to remember though that the flow is still unstably stratified, but with a much more uniform mean stratification than at the start of the experiment. At later times the flow becomes stably stratified as the densest fluid reaches the bottom of the tank. Stable stratification is apparent when $\tau - \tau_0 \approx 5$, and there is little subsequent change in the profile.

The fact that the final state, after all motion within the tank has ceased, is one in which the density stratification is stably stratified shows that the fluids do not mix completely. If mixing were complete the density throughout the tank would be uniform. Since the initial and final potential energies of the system can be determined from measurements, it is possible to determine the fraction η of the initial available potential energy which is used to mix the fluids. This 'mixing efficiency' η was measured as a function of the Atwood number A in LR and the value was found to increase with increasing A, attaining a value of $\eta = 0.35$. Figure 6 shows the calculated values of the box-averaged kinetic and potential energy loss as a function of the time $\tau - \tau_0$. Initially, both the kinetic and potential energy loss increase with time until, at about $\tau - \tau_0 = 6$, the potential energy stays roughly constant and the kinetic energy decreases. The constant value of the potential energy results from the fact that the stratification is no longer changing, and the kinetic energy decays due to dissipation. Similar results are obtained when the long-wave perturbation is present, although there is a decrease in both the maximum potential energy loss and kinetic energy achieved. The mixing efficiency η is defined as

$$\eta = 1 - P/P_{max}, \tag{5.1}$$

where P is the final potential energy loss and P_{max} is the change in potential energy if the fluids interchange positions without any mixing (i.e. all the upper-layer fluid eventually occupies the lower layer, and its density is unchanged). The values of η for the cases shown in figure 6 are 0.48 (random initial perturbation) and 0.47 (with long-

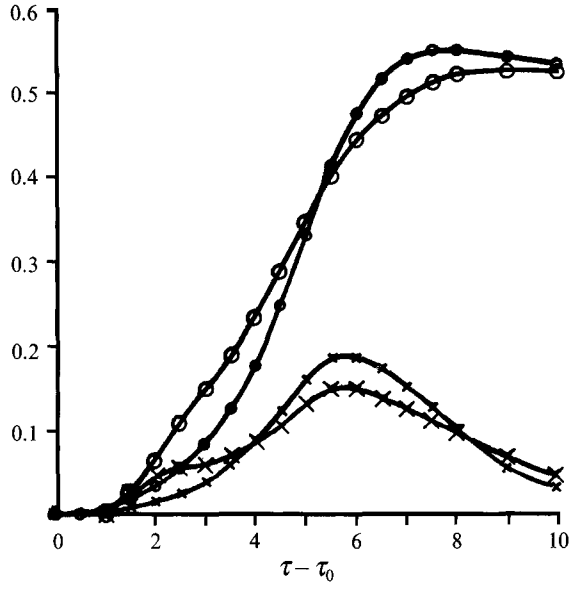

FIGURE 6. Total kinetic energy (crosses) and change in potential energy (circles) plotted against dimensionless time $\tau-\tau_0$, for numerical calculations with (small symbols) and without (large symbols) the long-wave perturbation.

wave perturbation). These results are both significantly higher than the laboratory values. Large-scale overturning motions, which may arise from the circulation induced by the removal of the barrier, were observed in the laboratory experiments at later times. These motions may have reduced the mixing efficiency in the experiments.

6. Quantitative comparison: local properties

6.1. *Concentration fluctuations*

Concentration fluctuations were measured by conductivity probes at fixed positions in the tank. Examples of the records from these probes and discussion of the performance of the probes may be found in LR. Here we present some results from these measurements and compare them with the equivalent results from the numerical calculations.

The r.m.s. concentration fluctuation $\sigma(\tau)$ is given by

$$\sigma(\tau) = \frac{1}{\Delta\tau}\int_{\tau-\frac{1}{2}\Delta\tau}^{\tau+\frac{1}{2}\Delta\tau} \frac{(\rho(\tau')-\bar{\rho})^2}{\rho_1-\rho_2}\,\mathrm{d}\tau', \tag{6.1}$$

where $\rho(\tau)$ is the density measured at a point and

$$\bar{\rho} = \frac{1}{\Delta\tau}\int_{\tau-\frac{1}{2}\Delta\tau}^{\tau+\frac{1}{2}\Delta\tau} \rho(\tau')\,\mathrm{d}\tau'$$

is the time running mean of the density. The value of the averaging time was chosen to be $\Delta\tau = 0.66$, and the results are insensitive to small variations about this value (see LR).

Figure 7 shows $\bar{\sigma}$, which is the horizontal average of $\sigma(\tau)$ at $z = 0.05$ above the mid-plane of the tank, as a function of time. The numerical results (figure 7*a*) are averages over an array of 8×8 coplanar probe positions. The experimental results (figure 7*b*) are obtained by ensemble averages over 10 experiments each of which contain five

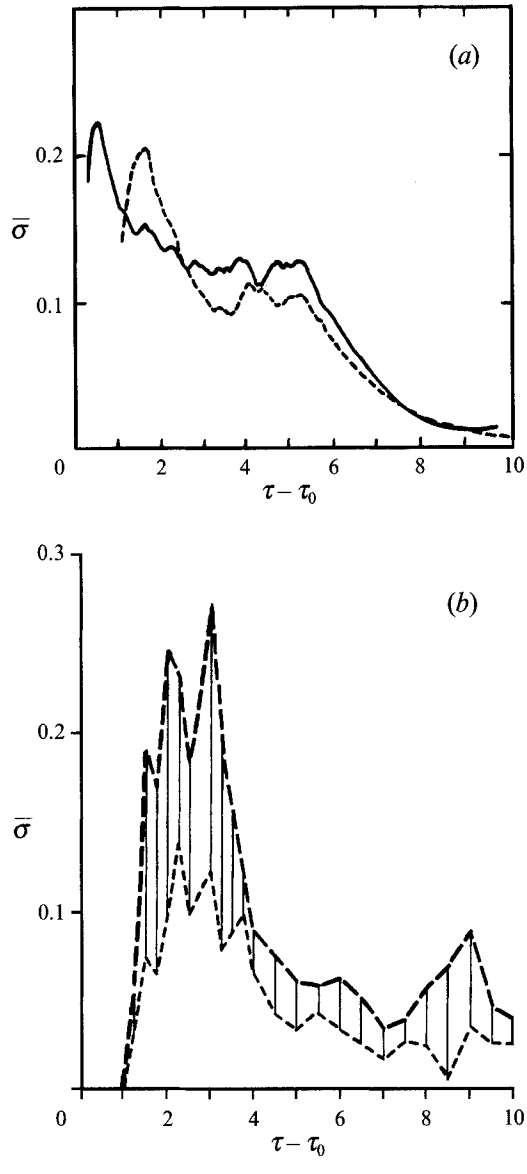

FIGURE 7. The r.m.s. concentration fluctuation $\bar{\sigma}(\tau)$ plotted against $\tau-\tau_0$. The numerical calculations are shown in (*a*) with those including the long-wave perturbation shown as the dashed curve. The experimental results, shown as a range corresponding to one standard deviation either side of the ensemble average, are given in (*b*).

measurement positions in the plane, and one standard deviation either side of the average values are shown. Experiments and numerical simulations both give peak values for $\bar{\sigma}$ of about 0.2, although the peak values are achieved somewhat later in the experiments. There is approximate agreement for the timescale of the decay of the concentration fluctuations.

Figure 8 shows $\bar{\sigma}_{max}$, the ensemble of the plane averages of the maximum r.m.s. concentration fluctuation determined from (6.1), at different heights above the initial interface. There are significant differences between the calculations with and without the long-wave perturbation, especially near the interface where larger values are

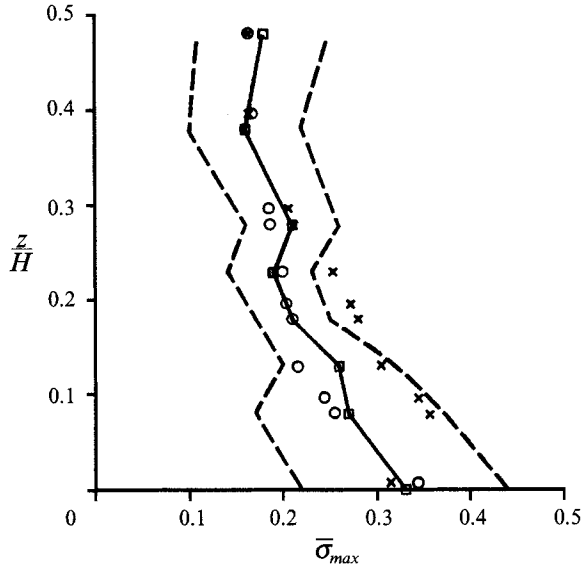

FIGURE 8. The maximum r.m.s. concentration fluctuation $\bar{\sigma}_{max}$ as a function of height. The experimental results (□) are shown with dashed lines are one standard deviation either side of the mean value. The numerical results are shown for the random initial perturbation (○), and with the addition of the long-wave perturbation (×).

obtained when the long wave is included. This increase implies less mixing (intermingling of two fluids without mixing would give $\bar{\sigma}_{max} = 0.5$) and is consistent with the observations of the mass fraction given in figure 5 which suggest that the initial perturbation is too coherent in this case. Both sets of numerical results lie within the experimental results, although better agreement is obtained without the long-wave perturbation.

The concentration f_2^{max}, which corresponds to the ensemble of plane averages of maximum proportion of lower-layer fluid recorded at a fixed position in the upper layer during the course of the experiment, and the corresponding quantity from the numerical calculations is shown in figure 9. The values have been normalized so that

$$f_2^{max} = \frac{\rho_1 - \rho_{min}(\tau)}{\rho_1 - \rho_2}, \tag{6.2}$$

where $\rho_{min}(\tau)$ is the minimum density recorded at the given height. If undiluted lower-layer fluid passes the measurement point (which is in the upper layer) then $f_2^{max} = 1$. On the other hand $f_2^{max} = 0$ when no lower-layer fluid passes the measurement position.

The variation with the long-wave perturbation is small, and both are consistent with the experimental data. The agreement with the experiments is excellent near the interface, but the theoretical values underestimate the measurements of greater distances. The experimental results suggest that f_2^{max} attains a reasonably constant value of about 0.3. This result is consistent with the detailed observation given in RL that the mixing takes place around the edges of the penetrating parcels of fluid, and that in the centre of the rising parcels only partial mixing has occurred. Nevertheless, by the time the parcels have reached the top of the tank, both the experiments and calculations show that significant mixing has taken place.

Probability density functions (p.d.f.s) of the density fluctuations are shown in figure

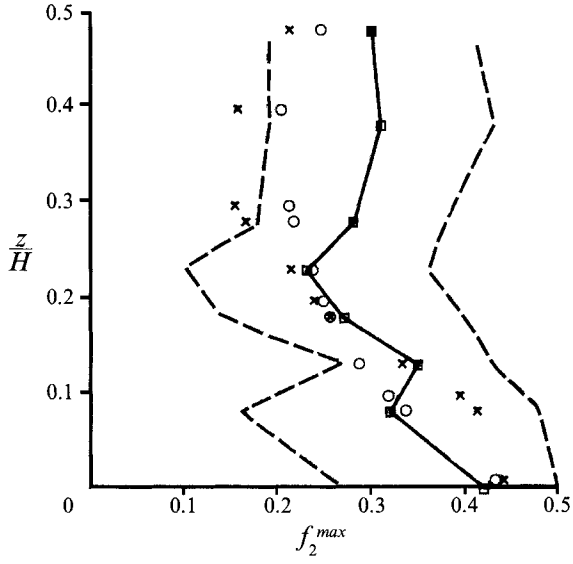

FIGURE 9. The maximum concentration f_2^{max} of lower-layer fluid recorded in the upper layer, at various distances above the initial interface. The symbols are the same as in figure 8.

10. The numerical results shown in figure 10(*a*) are obtained from concentration values in the centreplane at $\tau-\tau_0 = 2.5$. The experimental p.d.f. shown in figure 10(*b*) is calculated at the centreplane of the tank, from concentration measurements over the time interval $1 < \tau-\tau_0 < 3$. The observed p.d.f. is closer to the numerical results without the long-wave perturbation. The coherent form of the long-wave perturbation gives rise to large-scale vortices in the centreplane which appear to enhance the decay of density fluctuations at $z = 0$ for the time shown here. These distributions show that there is little unmixed fluid in the middle of the mixing zone, and support the previous observations that significant molecular mixing takes place during this period.

6.2. *pH measurement*

Measurements of mixed product were obtained by determining the reduction in light intensity resulting from the colour change of the pH indicator in the lower fluid. The results of these measurements are given in figure 11, which shows the concentration $\bar{C}$ averaged over the horizontal mid-plane of the tank as a function of $\tau-\tau_0$ for a range of different values of f_0. This value of f_0 gives the fraction of the two fluids that need to mix in order to produce the required pH for the colour change. For example, $f_0 = 0.1$ means that 10% of upper-layer fluid mixed with 90% of the lower-layer fluid will produce a colour change. The results have been normalized so that complete mixing of all fluid in the tank gives a value of $\bar{C} = C_0$. In the numerical calculations the concentration of coloured product was defined by

$$\bar{C} = \begin{cases} 2C_0(1-f_1), & f_1 > f_0, \\ 0, & f_1 \leqslant f_0. \end{cases}$$

The calculated values without and with long-wave perturbation are shown in figures 11(*a*) and 11(*b*), respectively, and the experimental results are given in figure 11(*c*).

Good general agreement is seen among all three sets of results. The value of $\bar{C}$ increases with τ and asymptotes to $\bar{C} = 1$ at large times. The initial rate of increase decreases with increasing f_0, which reflects the fact that a larger fraction of the two fluids must mix in order to achieve the same colour change. The effects of the long-

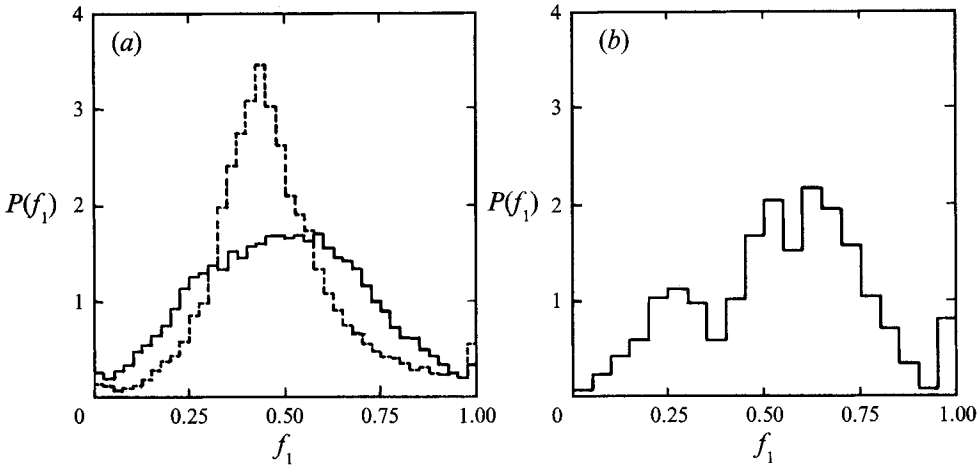

FIGURE 10. Probability density distributions for the concentration f_1 at the centreplane of the flow. The numerical results with (---) and without (—) the long-wave perturbation are shown in (*a*), and the experimental results are shown in (*b*).

wave perturbation is to alter the initial behaviour ($\tau - \tau_0 < 1$) and to cause a reduction in $\bar{C}$ around $\tau - \tau_0 = 4$. This reduction is not observed in the experimental results. We note also that for $f_0 = 0.1$ the mixing is complete at the mid-plane by about $\tau - \tau_0 = 3$ when the growing front has reached the bottom of the tank, consistent with the p.d.f. shown in figure 10.

Figure 12 shows mixed product $\bar{C}$ for $f_0 = 0.1$ as a function of depth for the non-dimensional times $\tau - \tau_0 = 1$, 2 and 3. The central plane of the tank could not be analysed owing to the shadow of the plate positioning slots and thus no experimental data are shown in that region in figure 12(*c*). The width of the mixed-product region agrees with that derived from the dye measurements, and there is on the whole good agreement with the numerical calculations although the experiments do not show the asymmetry of the numerical calculations. The calculation with the long-wave perturbation underestimates the amount of coloured product at $\tau - \tau_0 = 1$ owing to the coherent nature of the initial perturbation.

6.3. *Fractal dimension*

The fractal dimension of the 90 % iso-concentration contour was calculated from both the experimental and numerical results and the results are shown in figure 13. A box-counting algorithm was used and the fractal nature of the interface determined. It was observed, as can be seen in figure 13(*a*), that the fractal dimension increases with $\tau - \tau_0$ from 1.0 to a maximum value of 1.3 before decreasing again as stable stratification is established. (The fractal dimension determined by this method is a projection on to a plane, and so the actual fractal dimension is the quoted values plus one.)

The development of the full fractal structure takes approximately 1 to 2 non-dimensional time units. At earlier times only the linear Rayleigh–Taylor scales and the disturbances imposed by the withdrawal of the plate are present. The fractal dimension then remains approximately constant until the influence of the bottom of the tank and the subsequent stable stratification reduces the dimension again. The laser-induced fluorescence visualization method is restricted by the width of the laser sheet. Thus we are unable to resolve motions on scales less than 2 mm, which exceeds the Kolmogorov scale. On the other hand, as noted earlier the smallest scales observed initially at the

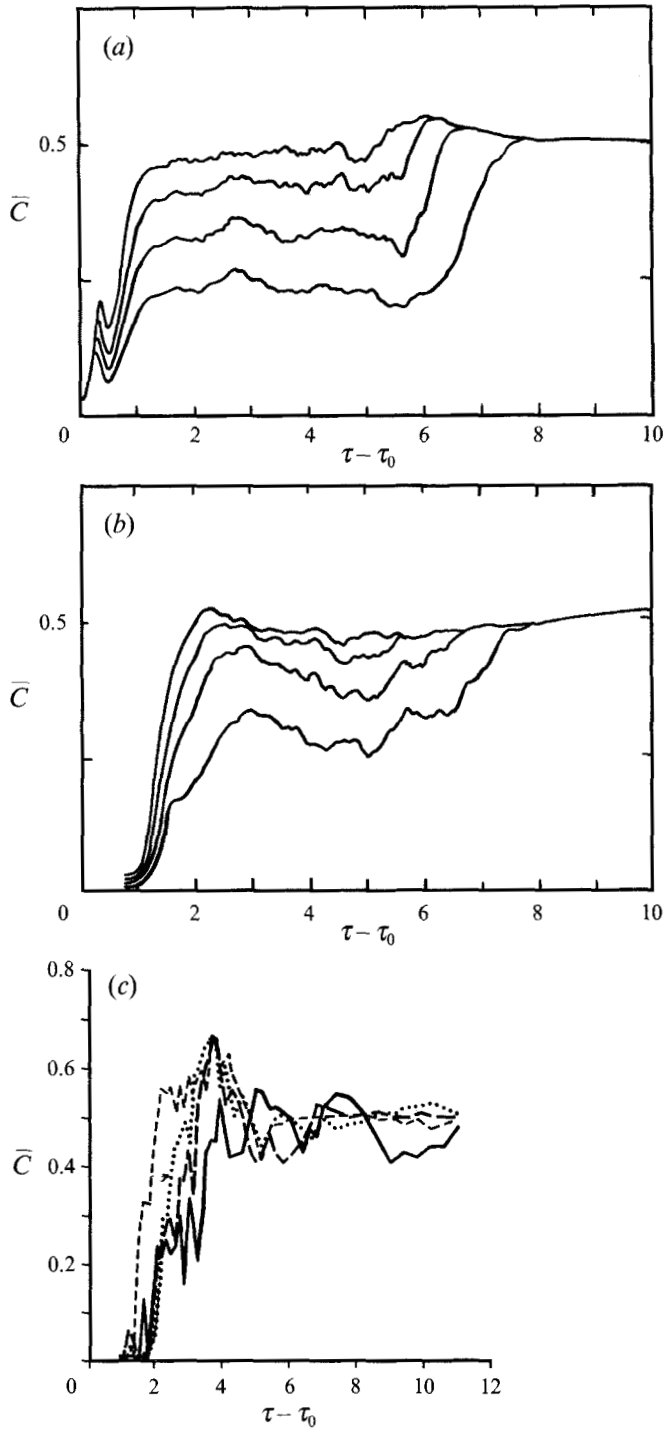

FIGURE 11. The concentration $\bar{C}$ of mixed product averaged over the centreplane as a function of time. The concentration has been normalized by C_0, the value when all the fluid is completely mixed. Plots are shown for four values of f_0 (0.1, 0.2, 0.3, 0.4) the fraction of upper-layer fluid required for a colour change, for the numerical results without and with the long-wave perturbation in (*a*) and (*b*), respectively, and the experimental results in (*c*).

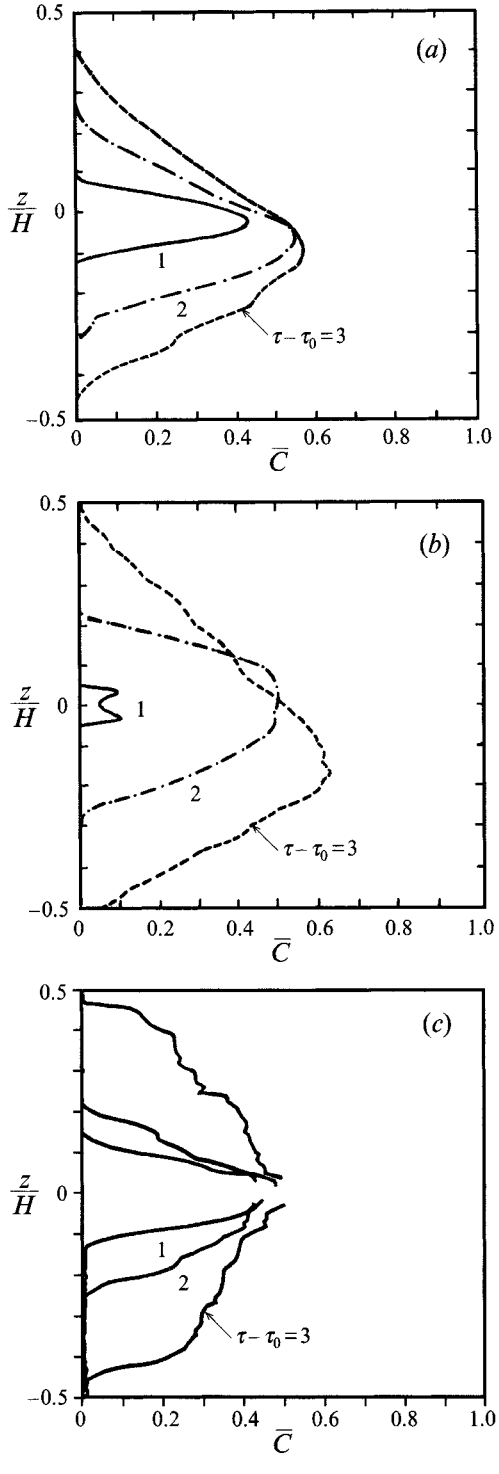

FIGURE 12. Depth profiles of the mixed product $\bar{C}$ averaged over horizontal plates at $\tau-\tau_0 = 1, 2, 3$. The numerical results without and with the long-wave perturbation are shown in (*a*) and (*b*), respectively, and the experimental results are shown in (*c*).

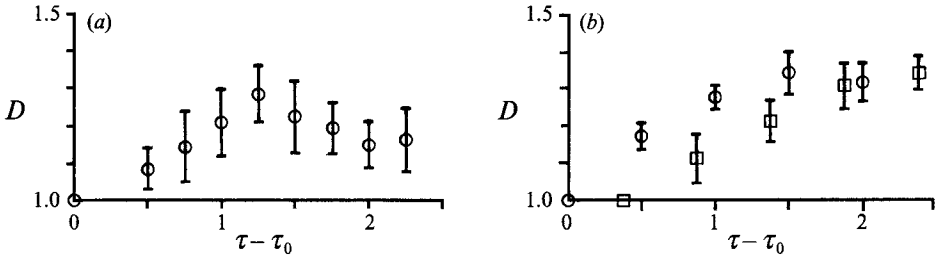

FIGURE 13. The fractal dimension D plotted against dimensionless time $\tau-\tau_0$. The experimental results are given in (a) and the numerical results, with (□) and without (○) the long-wave perturbation, are shown in (b).

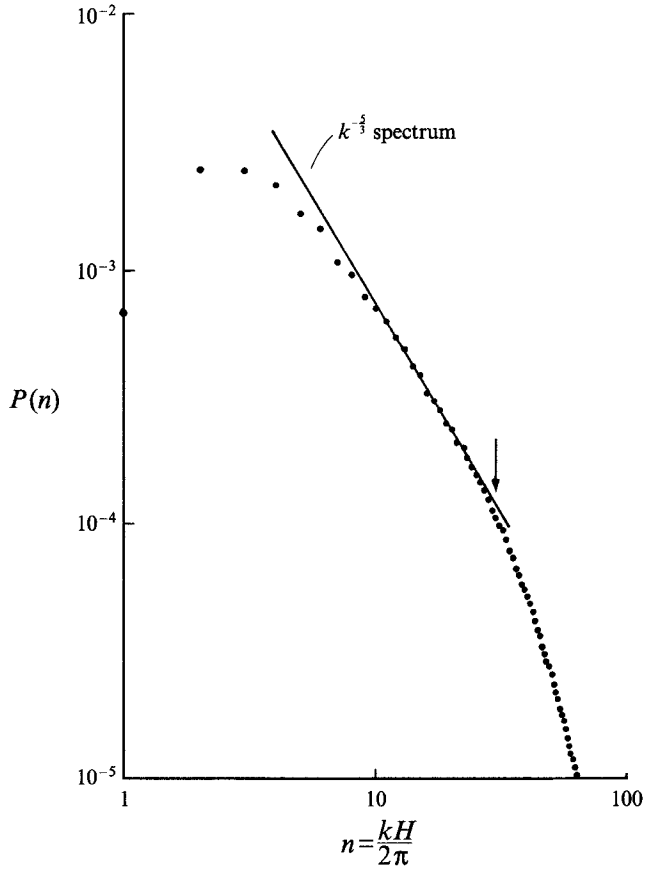

FIGURE 14. Power spectrum $P(n)$ for concentration fluctuations at $\tau = 3$ from the numerical calculation without the long-wave perturbation. The line drawn corresponds to a $k^{-\frac{5}{3}}$ spectrum, where $k = (k_x^2+k_y^2)^{\frac{1}{2}}$. The arrow indicates the point where the wavelength $2\pi/k$ equals 6 mesh widths.

interface edge were larger than the 2 mm resolution scale suggesting that the flow is not fully developed until after some time. The non-dimensional time for the front to reach the bottom of the tank is approximately 3τ, but at least 1τ is needed for the flow to become turbulent. This can be thought of as a transition between the initial growth dominated by the bubble competition and the fully turbulent regime.

The same box-counting algorithm was applied to the volume fraction isolines obtained from the numerical calculations. Elevation views were analysed at the non-dimensional times 1, 2, 3 and 4, giving values comparable with the experiments. Figure 13(*b*) shows the evolution of the fractal dimension in cases of both the random initial perturbations (circles) and with the long-wave perturbation (squares). There is good agreement between the numerical and experimental results in the early stages of the flow. The numerical results do not show the subsequent reduction in the dimension observed in the experiments.

Figure 14 shows a power spectrum for concentration fluctuations obtained from the numerical results at $\tau-\tau_0 = 3$. Two-dimensional Fourier analysis has been applied to each plane of numerical data and the resulting power values have been averaged in the vertical direction. The numerical results are consistent with a $k^{-\frac{5}{3}}$ spectrum at high wavenumbers. However, the power law cannot be conclusively verified as the numerical resolution is insufficient. This slope of the spectrum is consistent with the values of the fractal dimension measured at $\tau-\tau_0 = 3$.

7. Numerical simulation of the self-similar mixing process

The consistency between the three-dimensional simulations and the experimental results give confidence in the numerical technique. However, the results clearly show that the long-wave perturbation significantly enhances the growth of the mixing zone, and the similarity solution in which loss of memory of the initial conditions occurs is not achieved in the experiments. It is therefore of value to use numerical simulation to estimate the properties of this similarity solution. A modified computational mesh has been used for this purpose. Extra coarsely zoned layers of thickness $0.15H$ with 10 coarse zones were added to the top and bottom of the tanks to reduce the effect of the boundaries on the growth of the mixing zone. The horizontal cross-section was reduced to $0.8H \times 0.8H$; this size was considered sufficient as the overturning phase is not being computed. The mesh size used was $168 \times 168 \times 230$. Calculations were run to $\tau = 3.5$ when the mixing zone width $\delta \sim H = 210$ zones. As for the previous calculations the density ratio used as $\rho_1/\rho_2 = 1.5$. The initial random perturbation had standard deviation $\sigma = 0.08\Delta x = 4 \times 10^{-4} H$.

Properties of the mixing zone are given at $\tau = 3.25$. Figure 15 shows profiles for plane-averaged values of the fluid-1 volume fraction, the vertical and horizontal components of kinetic energy per unit mass and the molecular mixing fraction. The volume fraction profile is similar to those observed in the experiments (see figure 5). The kinetic energy components are defined as $k_z = \frac{1}{2}\overline{\rho w^2}/\bar{\rho}$ (vertical) and $k_h = \frac{1}{4}\overline{\rho(u^2+v^2)}/\bar{\rho}$ (horizontal). Both quantities show a peak in the middle of the mixing zone. The peak value for the vertical component is about three times the peak value for the horizontal component reflecting the anisotropy of the buoyancy-driven motions. The molecular mixing fraction, θ, is defined in the same way as in Youngs (1991), i.e.

$$\theta(z) = \frac{\overline{f_1 f_2}}{\bar{f}_1 \bar{f}_2} = 1 - \frac{\sigma^2}{\bar{f}_1 \bar{f}_2},$$

where $\sigma^2 = \overline{(f_1 - \bar{f}_1)^2}$. The quantity $1-\theta$ corresponds to the intensity of segregation used by Dankwerts (1952). It is observed that θ is approximately uniform across the mixing zone but that there is some reduction in θ with height. This is due to the slight deviation from the Boussinesq approximation at the density ratio of $\rho_1/\rho_2 = 1.5$ used in the simulations. In the middle of the mixing zone θ is about 0.8. In the experiments

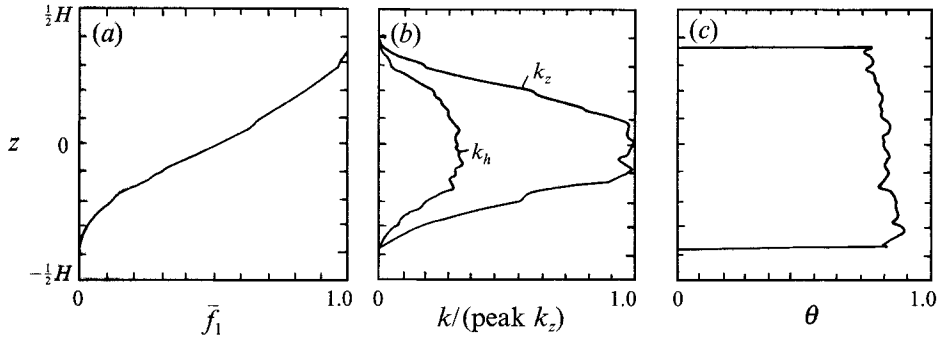

FIGURE 15. Plane-averaged quantities at $\tau = 3.25$: (*a*) fluid-1 volume fraction, f_1; (*b*) vertical and horizontal components of kinetic energy per unit mass, k_z and k_h; (*c*) molecular mixing fraction, θ.

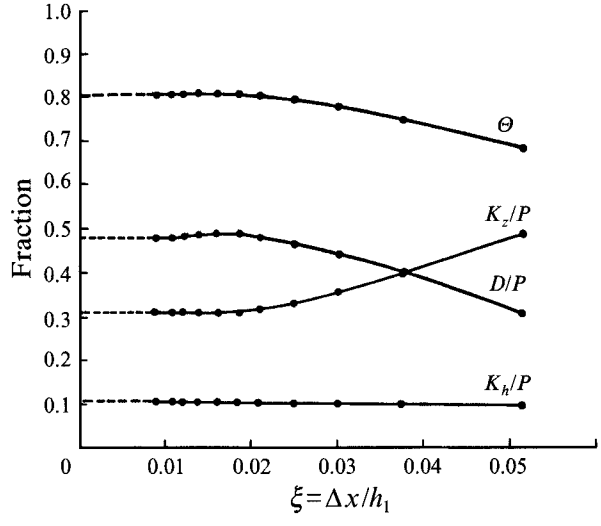

FIGURE 16. Time variation of layer-integrated quantities: molecular mixing fraction, Θ, vertical and horizontal components of kinetic energy; K_z and K_h and dissipation, D.

the concentration fluctuation σ is defined somewhat differently. However, if the differences in definition are ignored, the observed values of $\bar{\sigma}_{max} \sim 0.25$ (figure 8) imply a molecular mixing fraction of $\theta = 1 - 0.25^2/0.5^2 = 0.75$, which is consistent with the computed value.

The variation with time of quantities integrated over the whole mixing zone is shown in figure 16. Values are plotted against $\xi = \Delta x/h_1$, which is a measure of the numerical resolution of the mixing zone. As in Youngs (1991), the molecular mixing fraction for the whole mixing zone is defined as

$$\Theta = \int \overline{f_1 f_2}\, \mathrm{d}z \Big/ \int \bar{f}_1 \bar{f}_2\, \mathrm{d}z.$$

As the mixing zone becomes better resolved Θ tends to increase. However, there is little difference in the values at $\xi = 0.02$ ($h_1 = 50$ meshes) and $\xi = 0.01$ ($h_1 = 100$ meshes). Extrapolation to $\xi = 0$ indicates $\Theta = 0.81$ for the similarity solution. Also shown are the horizontal and vertical components at the kinetic energy, $K_z = \frac{1}{2}\int \rho w^2\, \mathrm{d}V$ and $K_h = \frac{1}{2}(K_x + K_y)$, and the kinetic energy dissipated, D. The quantities plotted are

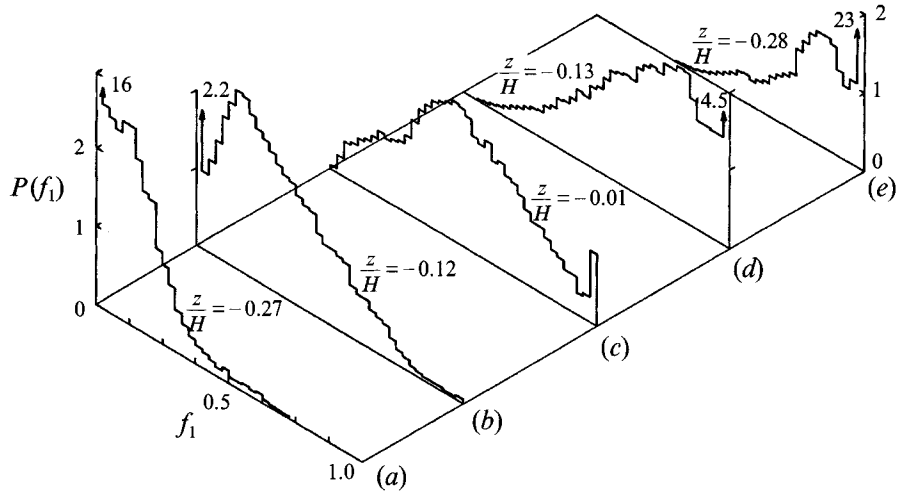

FIGURE 17. Probability distribution functions for various horizontal layers at $\tau = 3.25$.

divided by P, the loss of potential energy, which should equal $D+K_z+2K_h$. For the similarity solution these ratios should approach constant values. The graphs show that an approximate self-similar state is reached after the bubble penetration, h_1 has reached 50 meshes. The best estimate of the energy balance for the similarity solution is

dissipation of kinetic energy:	$D/P = 0.48$,
vertical component of kinetic energy:	$K_z/P = 0.31$,
horizontal component of kinetic energy:	$K_h/P = 0.11$.

These values are a little different to those quoted in Youngs (1991) because of the improved mesh resolutions.

Figure 17 shows probability distribution functions for the fluid-1 volume fraction, f_1, for various horizontal plane sections at scaled time $\tau = 3.25$. These give insight into the behaviour of a 'bubble' of the lighter fluid 2 as it rises through the mixing zone. At the bottom of the layer there is pure fluid 2, i.e. the p.d.f. consists of a δ-function at the origin. As z increases, the light fluid entrains some of the heavier fluid and the δ-function at $f_1 = 0$ is reduced (figures 17*a* and 17*b*). When the parcel of light fluid has reached the middle of the mixing zone the δ-function at the origin has disappeared (figure 17*c*). In fact, in the centre of the mixing zone there is little pure fluid 1 or pure fluid 2 and the p.d.f. has a peak at around $f_1 = 0.5$, which agrees with the experimental results (figure 10). As the bubble of light fluid rises into the upper half of the mixing zone it entrains more and more of the heavier fluid (figures 17*d* and 17*e*). When the bubble has reached the point where $f_1 = 0.9$ (figure 17*e*) the light fluid has become well mixed with heavy fluid. Again this is consistent with the experimental results. Probes at the top of the tank recorded the average value of f_2^{max} to be about 0.3, i.e. the bubbles were mixed with at least 70% of the heavier fluid. In the Boussinesq limit the p.d.f. for f_1 at $+z$ should be the same as the p.d.f. for $1-f_1$ at $-z$. It is evident that, for the density ratio $\rho_1/\rho_2 = 1.5$ used in the simulation, there is some deviation from the Boussinesq limit.

Finally the growth of the mixing zone width is considered. In order to compare with the observed 'edge' of the mixing zone the bubble penetration h_1 is in this case measured to the point where $\bar{f}_1 = 0.99$. Figure 18 shows a plot of h_1/H versus τ^2. The

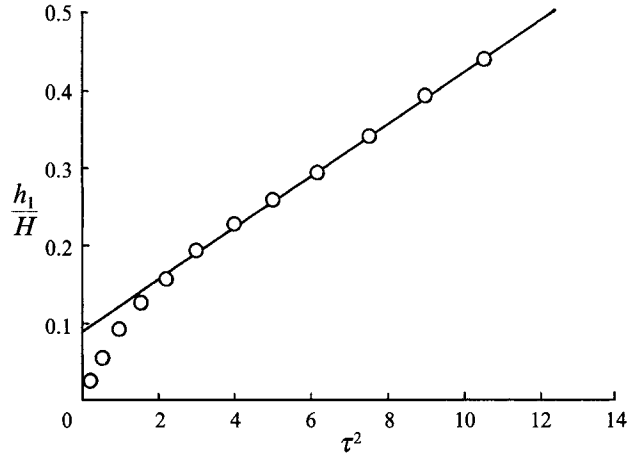

FIGURE 18. Bubble penetration, h_1 versus time squared. The line drawn has slope $\alpha = 0.033$.

slope of the graph gives the growth coefficient α, defined by (3.2). It is evident from figure 16 that dissipation of both density fluctuations and kinetic energy is underestimated in the early part of the calculation when $h_1 < 50$ meshes. This discrepancy is attributed to the inability to resolve the inertial range. As a result a high value of α is obtained at the start of the calculation. When the resolution of the mixing zone improves, the growth rate slows down and the slope of the graph at the end of calculation gives $\alpha_s = 0.033$ for the similarity solution. Other similar calculations gave α_s in the range 0.03 to 0.04. A similar trend has been noted by Glimm *et al.* (1990) in two-dimensional simulations of Rayleigh–Taylor instability using a front tracking method. In the early stage of the calculations, α was about 0.06; however, at a later stage, when the interface became highly convoluted and multiply connected, lower values, $\alpha = 0.038$ to 0.044, were reported. The experiments of Read (1984) and Youngs (1989), which gave $\alpha \sim 0.06$, used mainly immiscible fluids and surface tension may have inhibited fine-scale mixing thereby enhancing the growth of the mixing zone. There were no deliberately imposed perturbations in these earlier experiments. However, the meniscus on the walls of the tank perturbed the initial interface and this may have had some influence on the mixing rate. The present experimental results (§5) give $\alpha \sim 0.044$, if h_1 is measured to the point where $\bar{f}_1 = 0.95$, which is in better agreement with the calculated values.

The numerical estimates for α_s of about 0.035 should be treated with some caution as linear variation of h_1 with τ^2 is only seen for a period when h_1 increases by a factor 3. Finer-mesh calculations are needed for a more definitive estimate of α_s and this is not possible with present computer resources. If α_s is indeed as low as this then, according to the analysis described in §3, long-wave perturbations should enhance the mixing rate if $a_0/\lambda > 0.001$. In most experimental situations, controlling long-wavelength perturbations to this low level would be difficult. Hence complete loss of memory of the initial conditions in practical situations would not occur. This would have serious consequences for the application of turbulence models to Rayleigh–Taylor mixing problems, where model coefficients are adjusted to match the value of α. In the absence of a theoretical model relating α to the initial conditions, the only solution would be to adopt a pragmatic approach and adjust the turbulence model to give a typical observed value of α.

8. Conclusions

In this paper we have presented a comparison between time-dependent, three-dimensional numerical calculations of Rayleigh–Taylor instability and laboratory experiments of the same flow. Neither the numerical calculations nor the laboratory experiments are ideal, and the resulting comparison is a compromise in which we have tried to bring the two studies as close together as possible.

The numerical calculations are restricted by the fact that the smallest scales of the turbulent motion are not resolved. While the spectrum is consistent with a $k^{-\frac{5}{3}}$ decay, molecular mixing occurs on the smallest scales (for large Prandtl number) and so it is not obvious that the mixing process will be properly modelled by the numerical code.

The experiments are limited by the initial disturbances imposed by the withdrawal of the plate. These clearly have a significant effect on the initial stages of development of the flow, and we present arguments to suggest that this influence may continue throughout the growth of the mixing region. An attempt was made to represent this perturbation in the numerical calculations by introducing a long-wave disturbance and some enhanced small-scale perturbations into the initial conditions. The form of these initial disturbances was chosen by rather crude estimates of the effect of the plate withdrawal on the experiments, and it does not model all aspects of this complex process.

Generally, there is quite good agreement between the calculations and the experiments. We find that the motions are quite sensitive to the large scales produced when the barrier is removed, but that the amount of mixing is not. The details of the mixing process are changed in the early stages, but as three-dimensional small scales develop, the mixing is well represented in the model.

We are currently making a number of improvements to the barrier design and to measurements of the initial conditions in the experiments in an attempt to match them more closely to the numerical calculations.

This work is supported by the Ministry of Defence.

REFERENCES

ALLRED, J. C. & BLOUNT, G. H. 1953 Experimental studies of Taylor instability. *Los Alamos Natl Lab. Rep.* LA-1600.

ANUCHINA, N. N., KUCHERENKO, YU. A., NEUVAZHAEV, V. E., OGIBINA, V. N., SHIBARSHOV, L. I. & YAKOVLEV, V. G. 1978 Turbulent mixing at an accelerating interface between liquids of different densities. *Izv. Akad. Nauk. SSSR, Mekh Zhidk Gaza*, No. **6**, 157–160.

BELEN'KII, S. Z. & FRADKIN, E. S. 1965 Theory of turbulent mixing. *Fiz. Inst. Akad. Nauk. SSSR im P. N. Lebedev* **29**, 207–238.

CALDIN, E. F. 1964 *Fast Reactions in Solution.* Oxford: Blackwell.

CHERN, I.-L., GLIMM, J., MCBRYAN, O., PLOHR, B. & YANIV, S. 1986 Front tracking for gas dynamics. *J. Comput. Phys.* **62**, 83–110.

DAHLBURG, J. P. & GARDNER, J. H. 1990 Ablative Rayleigh–Taylor instability in three dimensions. *Phys. Rev.* A **41**, 5695–5698.

DALY, B. J. 1967 Numerical study of two fluid Rayleigh–Taylor instability. *Phys. Fluids* **10**, 297–307.

DANKWERTS, P. V. 1952 The definition and measurement of some characteristics of mixtures. *Appl. Sci. Res.* A **3**, 279–296.

DUFF, R. E., HARLOW, F. H. & HIRT, C. W. 1962 Effects of diffusion on interface instability between gases. *Phys. Fluids* **5**, 417–425.

EMMONS, H. W., CHANG, C. T. & WATSON, B. C. 1960 Taylor instability of finite surface waves. *J. Fluid Mech.* **7**, 177–193.

GLIMM, J., LI, X. L., MENIKOFF, R., SHARP, D. H. & ZHANG, Q. 1990 A numerical study of bubble interactions in Rayleigh–Taylor instability. *Phys. Fluids* A **2**, 2046–2054.

GRABOWSKI, W. W. & CLARK, T. L. 1991 Cloud-environment instability, rising thermal calculations in two spatial dimensions. *J. Atmos. Sci.* **48**, 527–546.

HARLOW, F. H. & WELCH, J. E. 1966 Numerical study of large-amplitude free-surface motions. *Phys. Fluids* **9**, 842–851.

KERR, R. M. 1988 Simulation of Rayleigh–Taylor flows using vortex blobs. *J. Comput. Phys.* **76**, 48–84.

LAYZER, D. 1955 On the instability of superposed fluids in a gravitational field. *Astrophys. J.* **122**, 1–12.

LEER, B. VAN 1977 Towards the ultimate conservative difference scheme IV. A new approach to numerical convection. *J. Comput. Phys.* **23**, 276–299.

LEWIS, D. J. 1950 The instability of liquid surfaces when accelerated in a direction perpendicular to their planes. *Proc. R. Soc. Lond.* A **202**, 81–96.

LINDEN, P. F. & REDONDO, J. M. 1991 Molecular mixing in Rayleigh–Taylor instability. Part I. Global mixing. *Phys. Fluids* A **3**, 1269–1277 (referred to herein as LR).

MOIN, P. & KIM, J. 1982 Numerical investigation of turbulent channel flow. *J. Fluid Mech.* **118**, 341–377.

PASSOT, T. & POUQUET, A. 1988 Hyperviscosity for compressible flows using spectral methods. *J. Comput. Phys.* **75**, 300–313.

READ, K. I. 1984 Experimental investigation of turbulent mixing by Rayleigh–Taylor instability. *Physica* **12D**, 45–58.

ROZANOV, V. B., LEBO, I. G., ZAYTSEV, S. G. *et al.* 1990 Experimental investigations of gravitational instability and turbulent mixing in stratified flows and acceleration fields in connection with the problem of Inertial Confinement Fusion. *Levedev Physical Institute preprint* 56, Moscow (in Russian).

TOWN, R. J. P. & BELL, A. R. 1991 Three-dimensional simulations of the implosion of inertial confinement fusion targets. *Phys. Rev. Lett.* **67**, 1863–1866.

TRYGGVASON, G. 1988 Numerical simulations of the Rayleigh–Taylor instability. *J. Comput. Phys.* **75**, 253–282.

TRYGGVASON, G. & UNVERDI, O. 1990 Computations of three-dimensional Rayleigh–Taylor instability. *Phys. Fluids* A **2**, 656–659.

YOUNGS, D. L. 1984 Numerical simulation of turbulent mixing by Rayleigh–Taylor instability. *Physica* **12D**, 32–44.

YOUNGS, D. L. 1989 Modelling turbulent mixing to Rayleigh–Taylor instability. *Physica* **D37**, 270–287.

YOUNGS, D. L. 1991 Three-dimensional numerical simulation of turbulent mixing by Rayleigh–Taylor instability. *Phys. Fluids* A **3**, 1312–1320.